American Mineralogist, Volume 108, pages 326–337, 2023

Isotopic responses of magnesium to two types of dissolution-reprecipitation processes for the growth of the double-carbonate mineral norsethite

Chuan Liu[1], Kai Wang[1], and Weiqiang Li[1,*]

[1]State Key Laboratory for Mineral Deposits Research, School of Earth Sciences and Engineering, Nanjing University, Nanjing, Jiangsu 210093, PR China

Abstract

An important mechanism of carbonate mineral growth is dissolution-reprecipitation, including the transformation of amorphous precursor to crystalline carbonates, and coarsening (ripening) of fine carbonate crystals. However, the mechanistic details of cation exchange associated with carbonate mineral growth via a dissolution-reprecipitation process are still not well understood. In this study, we used Mg isotopes to probe the exchange of Mg between aqueous solutions and norsethite [$BaMg(CO_3)_2$] by systematic synthesis experiments. Norsethite is a model double carbonate, with a general formula of $AB(CO_3)_2$, where A and B stand for two different divalent ions. Formation of norsethite is comprised of three stages, including: (1) precipitation of barium-magnesium (Ba-Mg) amorphous carbonate; (2) transformation of Ba-Mg amorphous carbonate to nano-crystalline norsethite by fast dissolution-reprecipitation; and (3) coarsening (ripening) of nano-norsethite by slow dissolution-reprecipitation. Magnesium isotopes displayed distinct fractionation behaviors in each of the three stages. The Mg isotope fractionation factors ($\Delta^{26}Mg_{solid\text{-}aq}$) associated with precipitation of Ba-Mg amorphous carbonate were slightly negative and temperature-dependent, from –0.83‰ at 30 °C to –0.53‰ at 70 °C. During the transformation of Ba-Mg amorphous carbonate to nano-crystalline norsethite, isotopically light Mg isotopes were further enriched in the solid phase, with apparent $\Delta^{26}Mg_{solid\text{-}aq}$ decreasing to –2.12‰ at 30 °C and –1.56‰ at 70 °C. In the ripening stage, norsethite became isotopically heavier, with $\Delta^{26}Mg_{solid\text{-}aq}$ increasing up to –1.95‰ at 30 °C and –1.17‰ at 70 °C. The experimental results show that non-equilibrium isotope fractionation occurred during the transformation of amorphous carbonate to nano-crystalline norsethite (i.e., fast dissolution-reprecipitation). By contrast, the subsequent ripening of the norsethite led to the evolution toward isotopic equilibrium of the system by slower exchange with a longer reaction time (i.e., slow dissolution-reprecipitation). Moreover, our first-principles calculation results indicate that the equilibrium isotope fractionation was approached, but not attained, even after 276 days of recrystallization at temperatures below 70 °C. In short, this study has identified two different types of dissolution-reprecipitation process during the carbonate mineral growth and highlights the importance of understanding formation mechanism and post-depositional history of carbonate in interpreting the isotopic data of carbonate minerals.

Keywords: Norsethite, amorphous carbonate, dissolution-reprecipitation, transformation, recrystallization, Mg isotope

Introduction

Carbonates comprise a major component of the ancient sedimentary records (e.g., Morse and Mackenzie 1990) and they are of great importance in geological record, as they document a variety of geological, environmental, and biological processes. Carbonate is a ubiquitous material and plays an essential role in human society, such as construction, agriculture, and mechanical engineering (e.g., Børja and Nilsen 2009; De Muynck et al. 2008; Gu et al. 2008; Jin and Yue 2008; Wang et al. 2021). For a better interpretation of carbonate geochemical records and industrial applications, it is important to understand the mechanism that controls carbonate nucleation and growth.

Carbonates could grow via different mechanisms. Numerous studies have been conducted to study the formation of carbonate minerals, focusing on the classic crystal growth mechanism of ion-by-ion attachment (e.g., Davis et al. 2000; De Yoreo et al. 2013; Hong et al. 2016; Nielsen et al. 2016; Teng et al. 2000). However, the formation of carbonate minerals could proceed via an alternative, yet fundamental pathway, which is the transformation of amorphous carbonate precursor (e.g., Giuffre et al. 2015; Liu and Li 2020; Loste et al. 2003; Mavromatis et al. 2017b; Rodriguez-Blanco et al. 2017), a kind of metastable material with the microscopic structure that lacks long-range order. Carbonate formation via the pathway of transformation of amorphous carbonate is particularly important for biomineralization. Phenomena of amorphous carbonate transformation have been reported in many biologically precipitated carbonates (Gower 2008 and references therein), such as foraminifera (Jacob et al. 2017; Mor Khalifa et al. 2018), coral skeletons (Mass et al. 2017;

* E-mail: liweiqiang@nju.edu.cn. Orcid 0000-0003-2648-7630

0003-004X/23/0002–326$05.00/DOI: https://doi.org/10.2138/am-2022-8386

Sun et al. 2020; Von Euw et al. 2017), sea urchin spicule (Politi et al. 2008; Raz et al. 2003), and mollusk shells (Baronnet et al. 2008; Weiss et al. 2002). Transformation of amorphous carbonate could take place via a coupled dissolution-reprecipitation mechanism (e.g., Giuffre et al. 2015; Liu and Li 2020; Purgstaller et al. 2016). Furthermore, once the carbonate minerals form, the recrystallization, which is one of the most fundamental changes for carbonates during the diagenesis process (Fantle et al. 2020), takes place by continuous dissolution-reprecipitation mechanism and will not stop until the minerals are completely isolated from surrounding fluids. Therefore, dissolution-reprecipitation is one of the key mechanisms governing the formation and growth of carbonate minerals. However, the nature and kinetics of atom/ion exchange during the dissolution-reprecipitation of carbonates are still not completely understood (Burdige et al. 2010; Gorski and Fantle 2017; Hu and Burdige 2007; Reeves and Rothman 2013; Zamanian et al. 2016). Yet dissolution-reprecipitation of carbonates exerts strong controls on the elemental and isotopic signatures of carbonates, which are vital information for a variety of applications, such as reconstructing the evolution seawater chemistry (pH, redox conditions, and chemical composition) (e.g., Bialik et al. 2018; Higgins and Schrag 2012; Rae et al. 2011; Ries 2004; Rollion-Bard et al. 2011; Zhang et al. 2018) and paleo-climate (e.g., Bice et al. 2006; Lachniet 2009; McDermott 2004; Mitsuguchi et al. 1996; Wang et al. 2001), as well as tracing the diagenesis process (Banner 1995; Derry et al. 1992; Swart 2015 and references therein).

Magnesium is a common component in carbonates and its isotopes have been applied to paleoenvironmental and paleographic studies (Crockford et al. 2021; Fantle and Higgins 2014; Gothmann et al. 2017; Higgins and Schrag 2012; Li et al. 2015; Liu et al. 2018; Pogge von Strandmann et al. 2014). Moreover, isotopes can provide unique information for mineral dissolution, precipitation, as well as ion exchange between minerals and fluids (e.g., Chanda et al. 2019; Frierdich et al. 2019; Gorski and Fantle 2017; Liu and Li 2020; Zhu et al. 2020). Therefore, Mg isotopes in carbonate hold a promise for elucidating some key aspects of the dissolution-reprecipitation process. In this study, we conducted systematic low-temperature (30 to 80 °C) synthesis experiments of norsethite [$BaMg(CO_3)_2$]. We documented the mineralogical characteristics of solid products and Mg isotope evolution of both mineral and coexisting solution. Norsethite is similar in crystal structure to dolomite and has been extensively studied to reveal the formation pathway of dolomite (Effenberger et al. 2014; Lindner and Jordan 2018; Pimentel and Pina 2014, 2016; Pimentel et al. 2021; Zhang et al. 2021). The experimental results, supplemented by ab initio calculations of equilibrium Mg isotope fractionation, reveal links between different carbonate mineral growth processes and Mg isotope fractionation behaviors and provide new insights about the fidelity of the Mg isotope ratios as a geochemical tool in carbonate records.

Experimental methods

Chemicals

For the experiments, gravimetrically weighted reagent grade salts of $MgCl_2·6H_2O$, $BaCl_2·2H_2O$, Na_2CO_3, and de-ionized water (18.2 MΩ·cm^{-1}), were used to prepare the reactant solutions. The reactant solutions include "solution A1" (2 M $MgCl_2$), "solution A2" (2 M $MgCl_2$ prepared from a different batch of $MgCl_2·6H_2O$ salt, which has different Mg isotope composition compared to "solution A1"), "solution B" (1 M $BaCl_2$), and "solution C" (1 M Na_2CO_3). All the experiments and subsequent analyses were conducted at the State Key Laboratory for Mineral Deposits Research, Nanjing University, China.

Synthesis experiments

The experiments were systematically performed at temperatures from 30 to 80 °C, with a 10 °C increment. For the main set of experiments (Set I), 5 mL of "solution A1," 5 mL of "solution B," and 15 mL of de-ionized water were mixed in a glass bottle to make a mixed solution that contained 0.4 M $MgCl_2$ and 0.2 M $BaCl_2$. On the other hand, 10 mL of "solution C" and 15 mL of de-ionized water were mixed in another glass bottle to make a solution of 0.4 M Na_2CO_3. The two bottles were capped and placed in an oven at a preset temperature (30, 40, 50, 60, 70, or 80 °C). Twelve hours of thermal equilibration was applied to ensure that the two solutions were at the desired temperature before the Mg-Ba solution was mixed with the Na_2CO_3 solution. Therefore, the initial reaction solution contained 0.2 M $MgCl_2$, 0.1 M $BaCl_2$, and 0.2 M Na_2CO_3. A white cloudy material appeared immediately upon mixing the two solutions. The reaction bottle was then tightly sealed by a rubber stopper and a clamped aluminum cap, and placed on a magnetically stirring hotplate that was set at different temperatures (30, 40, 50, 60, 70, or 80 °C). The temperature stability of the hotplate was monitored by an external temperature sensor that was attached to the bottom of the bottle and the temperature was found to fluctuate periodically. The amplitude of the measured temperature increased with the increase of the set temperature. For example, when the set temperature was 30 °C, the corresponding measured temperature ranged from 27.6 to 32.5 °C, and this value was between 72.1 and 89.1 °C when setting the temperature at 80 °C (Online Materials[1] Fig. S1 and Table S1). An aliquot of 5 mL homogeneous slurry was sampled by pipetting from the reactors after 1 min, 2 h, 1 day, 10 days, and 60 days of reaction time after mixing. The slurry was transferred into a centrifuge tube, which was centrifuged at 3000 r/min for 5 min to separate the solid and liquid phases, and the solid was further washed with de-ionized water and centrifuged three times to remove interstitial fluids. The supernatant was centrifuged at 12 000 r/min for 1 min before transfer to a second clean centrifuge tube. This operation was repeated three times to remove all the possible suspending solids from the aqueous solution. The washed solid was separated into different aliquots for elemental, mineralogical, and isotopic analyses.

Slightly different conditions were used in another set of experiments (Set II). In this experiment set, 2.5 mL of "solution A2," 2.5 mL of "solution B," and 20 mL of de-ionized water were mixed in a glass bottle to make a mixed solution that contained 0.2 M $MgCl_2$ and 0.1 M $BaCl_2$ at first, meanwhile, 5 mL of "solution C" and 20 mL of de-ionized water were mixed in another glass bottle to make a solution of 0.2 M Na_2CO_3. Then the Mg-Ba mixing solutions were mixed with Na_2CO_3 solutions, and the bottles were tightly sealed and placed on a magnetically stirring hotplate that was set at different temperatures (30, 40, 50, 60, 70, or 80 °C). Therefore, the initial reaction solution contained 0.1 M $MgCl_2$, 0.05 M $BaCl_2$ and 0.1 M Na_2CO_3. Sampling of 5 mL homogeneous slurry was conducted by pipetting from the reactors after 30 and 276 days of reaction time for this group of experiments. The solid and aqueous phases were separated by the same procedures as used in Set I.

Mineralogical analyses

A small aliquot of the solid product was prepared for scanning electron microscopy (SEM) observation and XRD analysis. SEM images were taken using a Carl Zeiss Supra 55 Field Emission Scanning Electron Microscope, and energy-dispersive X-ray spectroscopy (EDS) with the SEM was used for semi-quantitative analysis of the chemical compositions of the solids. Additionally, the specific surface area (SSA) of the samples was analyzed by the low-pressure nitrogen adsorption isotherm method (N_2-LPAI) at the MOE Key Laboratory Surficial Geochemistry at Nanjing University (details in Sun et al. 2017). Briefly, the measurements were conducted on a Micromeritics ASAP 2020 HD88 Surface Area and Porosity Analyzer. Before the measurements, the samples, except the amorphous carbonate, were heated in a vacuum oven at 378 K for 10 h for degassing. Then the N_2 adsorption-desorption, with the N_2 pressure from 0.05 to 0.2 atm, isotherm linear plots were obtained at 77.3 K. The SSA of samples were calculated using Brunauer-Emmet-Teller (BET) method with the isotherm linear plots.

XRD pattern of the solid product was obtained with a Rigaku RAPID II dual-source X-ray diffractometer using a rotating Mo ($K\alpha$ = 0.7093 Å) target X-ray source operated at 50 kV and 90 mA. The XRD pattern was collected using a two-dimensional image plate with a 10 min exposure time. Data interpretation was performed using a Rigaku 2DP program and Jade 6.5 software.

Solution chemistry characterization

The pH of solutions was measured using a Mettler Toledo combined electrode, which was calibrated by commercial standard buffers (pH = 4.00, 7.00, and 9.21 at 25 °C). The precision of each pH measurement was ±0.02 unit. An aliquot of the solution sample in synthesis experiments was taken for alkalinity measurement by titrating with 0.019 M HCl, and the titration operation was repeated three times; another aliquot was acidified with 2% HNO_3 for Mg^{2+} and Ba^{2+} analysis. Elemental concentration was measured by inductively coupled plasma optical emission spectroscopy (a Skyray ICP3000 type ICP-OES), using gravimetrically prepared multi-element standard solutions. The PHREEQC software was used to calculate the speciation of aqueous solutions, ion activities, and the saturation state of minerals with its Pitzer database. The solubility products for hydromagnesite (Gautier et al. 2014) and nesquehonite (Harrison et al. 2019) were included in the database. For all experiments, the pH values were measured at 25 °C and recalculated for the experimental temperature in PHREEQC. The saturation index (SI) of norsethite was expressed as:

$$\mathrm{SI} = \log(\Omega) = \log\left(\frac{\left(a_{\mathrm{Ba}^{2+}}\right)\left(a_{\mathrm{Mg}^{2+}}\right)\left(a_{\mathrm{CO_3^{2-}}}\right)^2}{K_{\mathrm{sp}}}\right) \quad (1)$$

where a represents the activity of an aqueous species, and the solubility product of norsethite is calculated using the function $\log_{10}K_{sp} = 31.007 - 7321.122/T - 0.0811 \times T$ (T in Kelvin, from 313 to 423 K) (Lindner et al. 2018).

Mg isotope analysis

Both solid and solution samples were treated with 1 mL concentrated nitric acid and evaporated on a hot plate at 95 °C. This operation was repeated three times to convert the salts to nitrate form for the column procedure. Then Mg of the solid and aqueous phases was purified following a well-established two-stage column procedure at the State Key Lab for Mineral Deposits Research, Nanjing University (Hu et al. 2017; Liu and Li 2020). Magnesium isotope analysis was performed using a Thermo-Scientific Neptune Plus multi-collector inductively coupled mass spectrometer (MC-ICP-MS) that operated on medium-mass-resolution, wet plasma mode, and the details of instrumental parameters are listed in Online Materials[1] Table S5. Instrument drift and mass bias were corrected using a standard-sample bracketing routine with an in-house Mg solution (HPS909104) as the bracketing standard (Hu et al. 2017; Li et al. 2015). Magnesium isotope data are reported using the standard δ notation (‰) of δ^{26}Mg and δ^{25}Mg for the $^{26}Mg/^{24}Mg$ and $^{25}Mg/^{24}Mg$ ratios relative to the DSM3 Mg isotope standard, where:

$$\delta^{x}\mathrm{Mg} = [(^{x}\mathrm{Mg}/^{24}\mathrm{Mg}_{\mathrm{sample}})/(^{x}\mathrm{Mg}/^{24}\mathrm{Mg}_{\mathrm{DSM3}}) - 1] \times 1000 \quad (2)$$

and the Mg isotope fractionation factor between two phases A and B is expressed as:

$$\Delta^{x}\mathrm{Mg}_{\mathrm{A\text{-}B}} = \delta^{x}\mathrm{Mg}_{\mathrm{A}} - \delta^{x}\mathrm{Mg}_{\mathrm{B}} \approx 10^{3}\ln\alpha^{x/24}_{\mathrm{A\text{-}B}} \quad (3)$$

where x = 25 or 26.

The external precision of the Mg isotope measurement was better than ±0.1‰ in δ^{26}Mg. Accuracy of Mg isotope analyses was monitored using pure Mg standards (Cambridge1 and DSM3), natural sample standards (IAPSO standard seawater), and a matrix-matching synthetic standard solution made of $BaCl_2$ and in-house Mg standard HPS932001 (1:1 molar ratio). The natural sample standards and matrix-matching synthetic standard were treated as unknown samples together with samples from experiments by ion-exchange chromatography, to assess the accuracy of the total chemical procedure, and the accuracy was verified to be better than ±0.1‰ in δ^{26}Mg, within the external precision. The measured Mg isotope compositions for both pure Mg standard and standard samples (matrix-matching synthetic standard and seawater) match well with published values (Online Materials[1] Table S5).

First-principles calculation of the equilibrium mass-dependent isotope fractionation

To better interpret the experimental data, equilibrium Mg isotope fractionation factors between norsethite, magnesite, and dolomite were calculated using ab intio methods. The isotopic fractionation factor between phase A and B is usually defined as $\alpha_{A\text{-}B} = \beta_A/\beta_B$, where β is the reduced partition function ratios or called β-factor. With the harmonic approximation, the β-factor of crystalline solids can be calculated by the following formula (Bigeleisen and Mayer 1947; Urey 1947):

$$\beta = \left[\prod_{i=1}^{3N_{\mathrm{at}}}\prod_{q}\frac{\nu^{*}_{q,i}}{\nu_{qi}} \times \frac{e^{-h\nu^{*}_{q,i}/(2kT)}}{1-e^{-h\nu^{*}_{q,i}/(kT)}} \cdot \frac{1-e^{-h\nu_{q,i}/(kT)}}{e^{-h\nu_{q,i}/(2kT)}}\right]^{1/N_q N} \quad (4)$$

where $\nu_{q,i}$ is the vibrational frequency of the ith phonon mode at the wavevector q, which can be derived from the first-principles calculation. N_{at}, N_q, and N represent the number of atoms in a unit cell, phonon wavevectors, and sites of isotopes in the unit cell, respectively. T is the temperature in Kelvin, h is Planck's constant, k is the Boltzmann constant, and the superscript * represents the vibrational frequencies of the system with heavier isotopes.

First-principles calculations were performed using the VASP package based on the projector-augmented-wave (PAW) method (Kresse and Joubert 1999). The exchange-correlation energies between electrons are described by the generalized gradient approximations (GGA) of the Perdew-Burke-Ernzerhof scheme for solids (PBEsol) (Perdew et al. 2008). Other functionals, such as PBE (Perdew et al. 1996) and local density approximations (LDA) (Perdew and Zunger 1981) are also tested. Pseudo-potentials of Ba_sv ($5s^25p^66s^2$), Ca_sv ($3s^23p^64s^2$), Mg_pv ($2p^63s^2$), C ($3s^23p^2$), and O ($2s^22p^4$) shipped with VASP are adopted, and plane-wave cutoffs are set to 600 eV. Conventional primitive cells of 30 atoms for norsethite $[Ba_3Mg_3(CO_3)_6]$, dolomite $[Ca_3Mg_3(CO_3)_6]$, and magnesite $[Mg_6(CO_3)_6]$ are first relaxed with variable lattices under the ambient pressure, and further atomic relaxations are performed with fixed cells. The Brillouin zone is sampled by a 3 × 3 × 1 k-points grid according to Monkhorst-Pack scheme (Monkhorst and Pack 1976). The convergence threshold for electronic iteration is 10^{-6} eV, and for structural relaxation, we choose when the residual forces act on atoms are $<10^{-4}$ eV/Å. To calculate the phonon frequencies needed in Equation 4, the Hessian matrix is constructed using the finite displacement method implemented in VASP using 2 × 2 × 1 supercells, and higher convergence tolerance of 10^{-7} eV/Å is also used to make sure the accuracy of the force calculation. Phonon frequencies are then obtained by using the PHONOPY (Togo and Tanaka 2015) package, and an 8 × 8 × 8 q-point mesh is proven sufficiently to get converged β-factors.

Results

Mineralogy

The mineralogy and key features of the XRD spectrum of the solid phases are summarized in Online Materials[1] Tables S2 and S3. In experiment Set I, the solid product sampled after 1 min of the reaction was pure Ba-Mg amorphous carbonate for experiments at 30 to 70 °C. However, for the experiment at 80 °C, the solid product sampled after 1 min of the reaction was a mixture of norsethite and Ba-Mg amorphous carbonate (Fig. 1a). The Ba-Mg amorphous carbonate occurred as spheres with a diameter of 20 to 200 nm irrespective of temperature (Figs. 2a and 2d; Online Materials[1] Fig. S3). The solid product at 80 °C consisted of Ba-Mg amorphous carbonate spheres and fine norsethite crystals below 50 nm (Fig. 2g). After 2 h of reaction, the amorphous carbonate completely transformed to norsethite in experiments between 40 to 80 °C, whereas the Ba-Mg amorphous carbonate persisted as the solid phase in the experiment at 30 °C (Online Materials[1] Table S2 and Fig. S2). After 1 day of reaction, the solid phase consisted of only norsethite in all experiments (Online Materials[1] Fig. S2). The crystals were anhedral and granular with a size below 50 nm for experiments between 40 to 70 °C (Online Materials[1] Fig. S4). In experiments performed at 30 and 80 °C, some larger crystals with more euhedral shapes were observed after 1 day. And after 60 days of reaction, the norsethite crystals became larger and more euhedral with rhombohedra morphology especially at higher temperatures (Figs. 2c, 2f, and 2i; Online Materials[1] Fig. S5). The increase of crystal size was also manifested by the decrease of the SSA of norsethite with a longer reaction time (Fig. 1b; Online Materials[1] Table S2).

XRD analyses confirmed that norsethite was the sole mineral

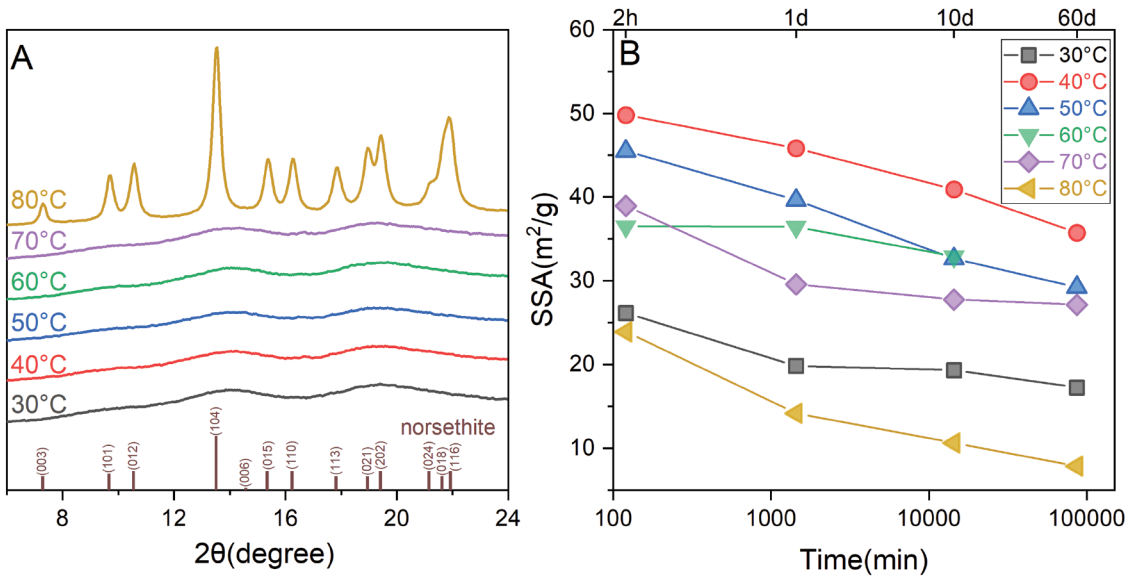

Figure 1. (**a**) XRD patterns of solid products after 1 min of reaction for experiment Set I. (**b**) Specific surface area (SSA) value of solid products vs. reaction time. (Color online.)

in the solid phase after the disappearance of Ba-Mg amorphous carbonate in all experiments (Online Materials[1] Fig. S2), consistent with a previous study conducted under similar conditions (Liu and Li 2020). Notably, the measured *d* value and the peak sharpness index (full-width at half maximum or FWHM) of the (104) peak for norsethite decreased with increasing reaction time (Figs. 3a and 3b; Online Materials[1] Table S2). The FWHM of dolomite (104) peak decreased with increasing crystallinity (Li et al. 2015), which was consistent with our SEM observation that the crystals became larger and more euhedral with increasing time (Fig. 1b). By contrast, the peak intensity ratios I(101)/I(012) and I(015)/I(110), indicators for the cation ordering in dolomite-group minerals (e.g., Li et al. 2015; Liu and Li 2020; Pimentel and Pina 2014), remained constant irrespective of reaction time (Figs. 3c and 3d).

Solution chemistry

The details of solution chemistry are tabulated in Online Materials[1] Table S4 for experiment Set I. Solutions sampled after 1 min of reaction had alkalinity ranging from 33 to 38 mM for experiments from 30 to 70 °C; however, the alkalinity of solution sampled after 1 min of reaction at 80 °C was much lower (11.5 mM). The alkalinity of solutions decreased to around 10 mM after 2 h for all experiments, except for the experiment conducted at 30 °C, where the alkalinity decreased to around 10 mM after 1 day. The decrease in solution alkalinity was temporally related to the disappearance of amorphous carbonate in the solid phase in the experiments. After the complete transformation of Ba-Mg amorphous carbonate to norsethite, the alkalinity of solutions fluctuated between 6 and 12 mM (Online Materials[1] Fig. S7a). The pH of the solutions generally increased when Ba-Mg amorphous carbonate transformed to norsethite for all experiments, then pH values decreased continuously with time (Online Materials[1] Fig. S7b).

The Mg concentrations ranged from 80 to 100 mM during the early period of reaction and decreased slightly with a longer reaction time (Online Materials[1] Fig. S7c). In contrast, the Ba concentrations were high (11 to 20 mM) in solutions sampled after 1 min of reaction and decreased rapidly to a value below 1 mM with increasing reaction time (Online Materials[1] Fig. S7d), which was coincident with the transformation of Ba-Mg amorphous carbonate. The concentration of Na^+, a "conservative element" in this experimental system, remained constant throughout the experiments at all temperatures (Online Materials[1] Fig. S7e). This indicates that the reaction bottles were well sealed and there was a negligible loss of water vapor throughout the experiments. In addition, the saturation index (SI) of norsethite decreased rapidly (Online Materials[1] Fig. S7f) after 1 day for the experiment at 30 °C and after 2 h for experiments from 40 to 80 °C, which corresponded to the transformation of Ba-Mg AC to norsethite. Then the downward trend gradually slowed down and the SI values became stabilized at around 1.5 (Online Materials[1] Fig. S7f), a state of oversaturation for norsethite.

Mg isotope results

In all experiments, $\delta^{26}Mg$ values of aqueous solutions were higher than those of the solid products (Table 1; Figs. 4a and 4b), corresponding to negative apparent Mg isotope fractionation factors ($\Delta^{26}Mg_{solid\text{-}aq}$) (Fig. 4c). Overall, the $\Delta^{26}Mg_{solid\text{-}aq}$ values were positively related to the reaction temperature. For experiment Set I, the $\Delta^{26}Mg_{solid\text{-}aq}$ between the freshly synthesized amorphous carbonate after 1 min of reaction and aqueous solution ranged from –0.83‰ at 30 °C to –0.53‰ at 70 °C, while the formation of norsethite at 80 °C resulted in a lower $\Delta^{26}Mg_{solid\text{-}aq}$ value (–1.27‰). The transformation of the Ba-Mg amorphous carbonate after 2 h of reaction time was accompanied by a significant decrease in the $\Delta^{26}Mg_{solid\text{-}aq}$ values, which varied from –1.83‰ at 40 °C to –1.56‰ at 70 °C. For experiment at 30 °C, the $\Delta^{26}Mg_{solid\text{-}aq}$ value remained nearly constant after 2 h due to the lack of Ba-Mg amorphous carbonate transformation, but after 1 day when the Ba-Mg amorphous carbonate was transformed to norsethite, the $\Delta^{26}Mg_{solid\text{-}aq}$ decreased to –2.12‰.

One striking observation is that, after the complete transformation of Ba-Mg amorphous carbonate to norsethite, the $\Delta^{26}Mg_{solid\text{-}aq}$ values began to increase continuously with time, and spanned from –1.95‰ to –1.04‰ after 60 days of reaction. Such increasing trend is confirmed in norsethite synthesis experiments Set II, in which the apparent $\Delta^{26}Mg_{solid\text{-}aq}$ also increased from –1.39‰ at 40 °C to –1.28‰ at 80 °C to –1.30‰ at 40 °C to –0.73‰ at 80 °C when the reaction time was extended to 276 days (Fig. 4d).

Ab initio calculation results

The calculated volumes of norsethite, dolomite, and magnesite are 379.02, 330.83, and 288.257 Å^3, respectively (Table 2), which are about 3% larger than experimental data [norsethite: 366.23 Å^3 (Effenberger and Zemann 1985); dolomite: 320.20 Å^3 (Markgraf and Reeder 1985); magnesite: 279.43 Å^3 (Markgraf and Reeder 1985)], while calculations using the two other functionals (LDA and PBE) predict smaller volumes. The calculated average Mg-O bond length in norsethite, dolomite, and magnesite are 2.082, 2.111, and 2.126 Å, respectively.

The calculated temperature dependence of β-factor is shown in Online Materials[1] Figure S6 and the polynomial fitting ($10^3 \ln\beta = d \times 10^6/T^2$) coefficients for norsethite, dolomite, and magnesite are 1.9424, 1.8653, and 1.8177, respectively (Table 2). The calculation results for two other functions are also listed. The calculated equilibrium fractionation between magnesite and dolomite is –0.53‰ at 298 K, which is consistent with Pinilla et al. (2015) and Gao et al. (2018). The equilibrium Mg isotope fractionation between norsethite and dolomite ($\alpha_{nor\text{-}dolo}$) can be calculated based on the calculated β-factors, which followed a function of $10^3\alpha_{nor\text{-}dolo} = -0.0771 \times 10^6/T^2$. This function can be combined with the temperature-dependent function for Mg isotope fractionation between dolomite and aqueous solution that was experimentally calibrated by Li et al. (2015), which leads to temperature-dependent function for Mg isotope fractionation between norsethite and aqueous solution (Fig. 5b):

$$\Delta^{26}Mg_{nor\text{-}aq} = -0.0783 \times 10^6/T^2 \quad (5)$$

where T is in Kelvin (K).

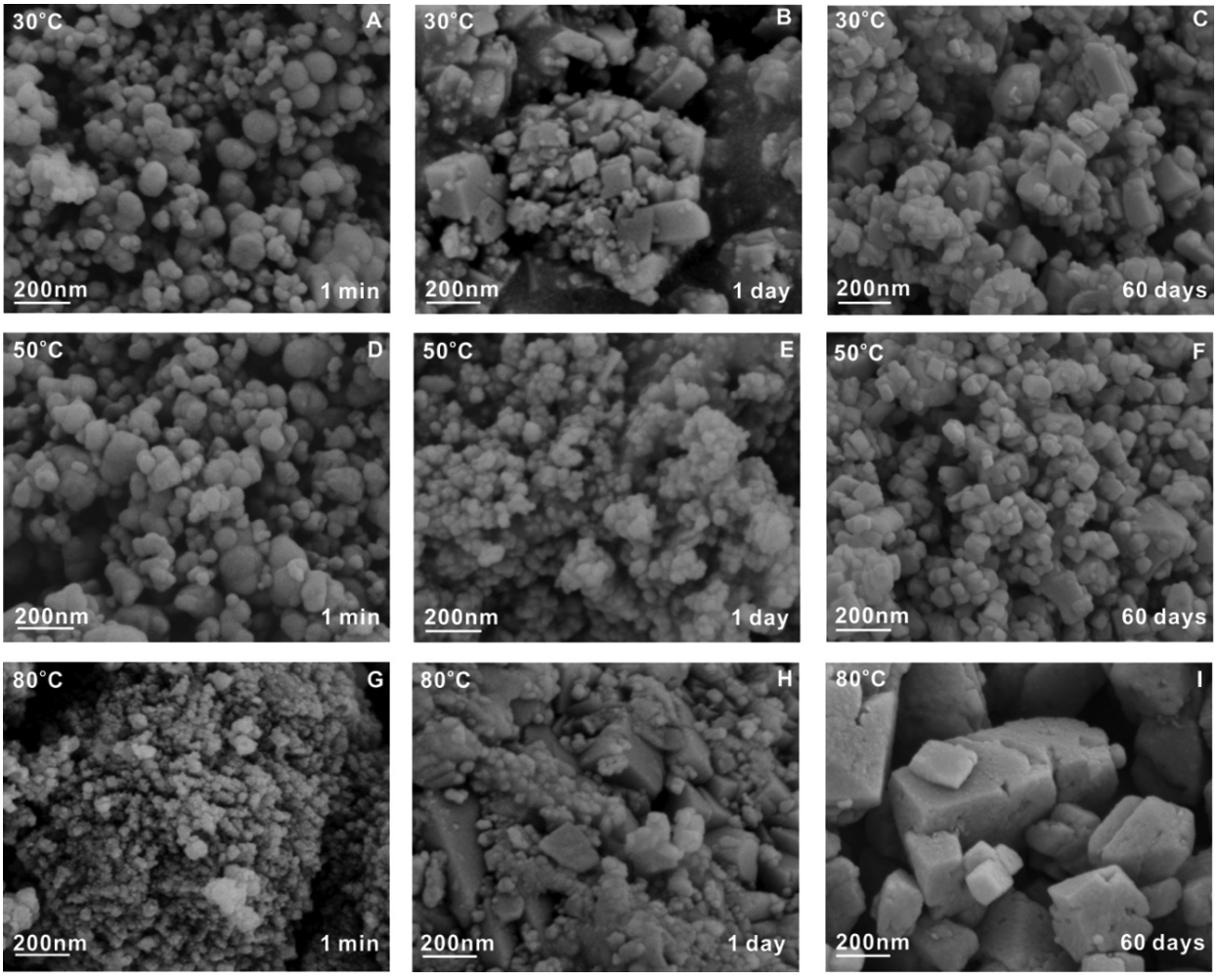

Figure 2. SEM images of the solid products for experiments Set I. For more details of the experimental conditions, see Online Materials[1] Table S2.

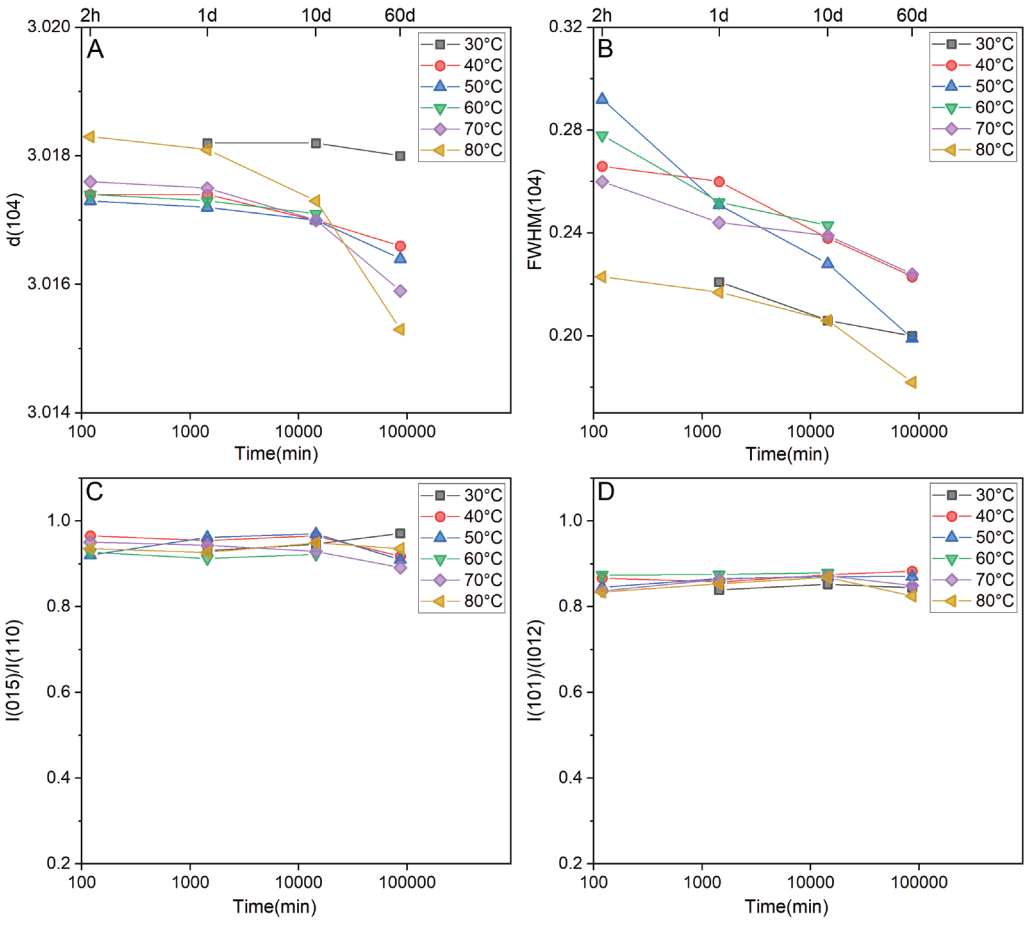

Figure 3. Lattice parameters of norsethite from the synthesis experiments Set I. (**a**) norsethite *d*(104) vs. reaction time; (**b**) FWHM of (104) peak for norsethite vs. reaction time; (**c**) I(101)/I(012) vs. reaction time; (**d**) I(015)/I(110) vs. reaction time. (Color online.)

Discussion

From our experimental results, the process of norsethite synthesis can be generalized and separated into three stages (Fig. 6): (1) the precipitation of Ba-Mg amorphous carbonate; (2) the transformation of Ba-Mg amorphous carbonate to nano-crystalline norsethite by fast dissolution-reprecipitation; and (3) recrystallization of nano-norsethite by slow dissolution-reprecipitation. Different stages of norsethite growth were accompanied by distinct Mg isotope fractionation behaviors. In experiment Set I, the first solid phase to appear in experiments at 30 to 70 °C was Ba-Mg amorphous carbonate only, despite that the initial mixed solution was highly oversaturated to various Mg- and Ba-bearing minerals. This can be attributed to the energy barrier for the formation of metastable amorphous carbonate being much lower than the formation of crystalline minerals (Gebauer and Cölfen 2011; Radha and Navrotsky 2013; Raiteri and Gale 2010). The spherical morphology of Ba-Mg amorphous carbonate observed in this study is remarkably similar to that of the synthesized amorphous calcium carbonate (ACC) reported in the literature (e.g., Xu et al. 2004). It should be noted that the first solid phase sampled from the experiment conducted at 80 °C was a mixture of Ba-Mg amorphous carbonate and nano-crystalline norsethite. This indicates that conversion of Ba-Mg amorphous carbonate to norsethite was extremely fast at 80 °C, occurring at a time scale similar to experimental manipulation for solid separation (i.e., 1 min). The $\Delta^{26}Mg_{solid\text{-}aq}$ between the amorphous carbonate after 1 min of reaction and aqueous solution ranged from –0.83‰ at 30 °C to –0.53‰ at 70 °C. Based on the calculation of speciation of Mg^{2+} in aqueous solution and the Mg isotope fractionation factors between different Mg species (Schott et al. 2016), the $\Delta^{26}Mg_{solid\text{-}Mg\_aq}$ between solid products and free aqueous Mg^{2+} (refer to Mg^{2+} only bonded to H_2O molecules) ranged from –0.54‰ at 30 °C to –0.34‰ at 70 °C (Online Materials[1] Table S6). The small magnitude of Mg isotope fractionation (–0.54‰ to –0.34‰) between amorphous carbonate and free aqueous Mg^{2+} may indicate that the Mg^{2+} is incorporated into the amorphous carbonate as the form of hydrated Mg. Actually, the dehydration of metal ion would lead to significant isotope fractionation (Hofmann et al. 2012) and this is consistent with that the water content is positively correlated to the Mg content in amorphous carbonate (Lin et al. 2015; Purgstaller et al. 2019).

The complete transformation of Ba-Mg amorphous carbonate to crystalline norsethite occurred within 2 h for experiments from 40 to 80 °C, while the Ba-Mg amorphous carbonate persisted at 30 °C until completely transformed to norsethite after 1 day. This suggests that temperature exerts a primary control on the transformation rate of amorphous carbonate for the norsethite

synthesis experiments in our study, which is consistent with the study of Liu and Li (2020). Based on XRD analysis, norsethite is the only crystalline mineral phase after the transformation of Ba-Mg amorphous carbonate (Online Materials[1] Table S2 and Fig. S2). It should be noted that other crystalline minerals, including northupite and witherite, have been reported to form during the analogous synthesis experiments of norsethite (Pimentel and Pina 2014, 2016). The different reaction pathways may be due to the different conditions used in these experiments. In this study, the molar ratio of $(Mg^{2+}+Ba^{2+}):CO_3^{2-}$ for reactants was above one, which means that the available CO_3^{2-} was limited to form other carbonate minerals. By contrast, that ratio was below one in the studies of Pimentel and Pina (2014, 2016). Additionally, the saturation index (SI) for witherite and northupite were below zero after the transformation of amorphous carbonate in this study (Online Materials[1] Table S4). This suggests that the formation pathways could depend on the solution chemistry, as has been implied in previous studies on the transformation of amorphous calcium carbonate (Lam et al. 2007; Loste et al. 2003; Purgstaller et al. 2017; Rodriguez-Blanco et al. 2012). It is interesting to note that the norsethite crystals obtained at 30 °C showed more euhedral crystal morphology and larger crystal size than that of norsethite obtained from 40 to 70 °C (Fig. 1b; Online Materials[1] Fig. S4). During the crystal formation process, the crystal size is considered to be positively correlated to the crystal growth rate, but negatively correlated to the crystal nucleation rate. These two competing mechanisms ultimately determine the crystal size distribution (Swanson 1977). The transformation rate of Ba-Mg amorphous carbonate for the experiment at 30 °C was slower than those in experiments at the higher temperatures (i.e., >1 day vs. <2 h), thus the experiment 30 °C should have been associated with slower nucleation rate, or less norsethite crystal nucleus,

TABLE 1. Mg isotope data of solution and solid phases in experiments

Expt. *T* (°C)	Time (min)	Solution					Solid					Fractionation (solid-aq)			
		$\delta^{26/24}$Mg	2SD	$\delta^{25/24}$Mg	2SD	n(N)[a]	$\delta^{26/24}$Mg	2SD	$\delta^{25/24}$Mg	2SD	n(N)[a]	$\Delta^{26/24}$Mg	2SD[c]	$\Delta^{25/24}$Mg	2SD[d]
Test solution[b]		−2.89	0.07	−1.48	0.04	12(4)									
Seawater		−0.79	0.06	−0.39	0.03	8(4)									
Solution A1		−1.04	0.05	−0.50	0.05	5(2)									
Solution A2		−3.39	0.14	−1.72	0.04	8(2)									
							Set I								
30	1	−0.59	0.06	−0.27	0.08	4(1)	−1.42	0.07	−0.70	0.04	5(1)	−0.83	0.10	−0.43	0.08
30	120	−0.59	0.08	−0.28	0.03	4(1)	−1.46	0.08	−0.73	0.03	5(1)	−0.88	0.11	−0.45	0.05
30	1440	0.05	0.00	0.05	0.01	2(1)	−2.07	0.03	−1.04	0.02	3(1)	−2.12	0.03	−1.09	0.02
30	14400	0.06	0.06	0.07	0.02	2(1)	−1.99	0.08	−0.99	0.02	2(1)	−2.05	0.10	−1.06	0.03
30	86400	0.00	0.09	0.03	0.04	2(1)	−1.95	0.03	−0.99	0.01	2(1)	−1.95	0.09	−1.02	0.04
40	1	−0.56	0.00	−0.25	0.03	2(1)	−1.34	0.01	−0.67	0.01	2(1)	−0.78	0.01	−0.42	0.03
40	120	−0.04	0.04	0.02	0.00	3(1)	−1.86	0.04	−0.93	0.02	4(1)	−1.83	0.06	−0.95	0.02
40	1440	−0.11	0.04	−0.02	0.02	4(1)	−1.78	0.08	−0.89	0.02	3(1)	−1.67	0.09	−0.87	0.03
40	14400	−0.13	0.04	−0.04	0.05	4(1)	−1.69	0.05	−0.84	0.03	5(1)	−1.55	0.06	−0.80	0.06
40	86400	−0.23	0.06	−0.11	0.00	2(1)	−1.63	0.03	−0.82	0.00	2(1)	−1.40	0.07	−0.71	0.00
50	1	−0.61	0.04	−0.28	0.03	2(1)	−1.32	0.07	−0.66	0.05	2(1)	−0.71	0.08	−0.37	0.06
50	120	−0.13	0.04	−0.03	0.02	2(1)	−1.80	0.03	−0.91	0.01	2(1)	−1.67	0.05	−0.87	0.02
50	1440	−0.21	0.01	−0.08	0.02	2(1)	−1.64	0.03	−0.82	0.03	2(1)	−1.43	0.03	−0.74	0.03
50	14400	−0.22	0.09	−0.08	0.05	4(1)	−1.70	0.01	−0.85	0.01	2(1)	−1.47	0.09	−0.76	0.05
50	86400	−0.32	0.02	−0.13	0.01	2(1)	−1.57	0.00	−0.80	0.04	2(1)	−1.25	0.02	−0.67	0.04
60	1	−0.65	0.09	−0.31	0.05	4(1)	−1.26	0.01	−0.63	0.02	2(1)	−0.61	0.09	−0.32	0.06
60	120	−0.13	0.03	−0.05	0.00	2(1)	−1.79	0.04	−0.88	0.01	2(1)	−1.66	0.05	−0.83	0.01
60	1440	−0.19	0.04	−0.07	0.05	2(1)	−1.63	0.03	−0.80	0.04	2(1)	−1.44	0.05	−0.73	0.06
60	14400	−0.27	0.03	−0.10	0.04	2(1)	−1.56	0.00	−0.79	0.06	2(1)	−1.29	0.03	−0.69	0.07
60	86400	−0.68	0.05	−0.32	0.02	2(1)	−1.13	0.02	−0.56	0.05	2(1)	−0.45	0.06	−0.24	0.05
70	1	−0.72	0.08	−0.33	0.05	3(1)	−1.24	0.04	−0.60	0.03	4(1)	−0.53	0.09	−0.27	0.06
70	120	−0.14	0.02	−0.05	0.01	2(1)	−1.69	0.06	−0.84	0.06	2(1)	−1.56	0.07	−0.79	0.06
70	1440	−0.22	0.07	−0.09	0.03	2(1)	−1.64	0.03	−0.82	0.01	2(1)	−1.42	0.08	−0.73	0.04
70	14400	−0.28	0.04	−0.12	0.05	2(1)	−1.58	0.01	−0.79	0.00	2(1)	−1.31	0.04	−0.67	0.05
70	86400	−0.31	0.02	−0.12	0.02	2(1)	−1.48	0.07	−0.71	0.03	2(1)	−1.17	0.08	−0.59	0.03
80	1	−0.32	0.01	−0.14	0.02	2(1)	−1.59	0.02	−0.78	0.04	2(1)	−1.27	0.03	−0.64	0.04
80	120	−0.01	0.01	0.04	0.01	2(1)	−1.83	0.07	−0.90	0.03	2(1)	−1.81	0.07	−0.94	0.03
80	1440	−0.12	0.06	−0.04	0.03	2(1)	−1.75	0.05	−0.87	0.01	2(1)	−1.62	0.08	−0.82	0.03
80	14400	−0.24	0.05	−0.09	0.04	4(1)	−1.60	0.08	−0.80	0.04	4(1)	−1.36	0.09	−0.71	0.06
80	86400	−0.41	0.05	−0.17	0.03	2(1)	−1.46	0.02	−0.71	0.00	2(1)	−1.04	0.05	−0.54	0.03
							Set II								
30	43200	−2.65	0.07	−1.34	0.03	5(1)	−4.08	0.01	−2.09	0.01	2(1)	−1.43	0.07	−0.75	0.03
30	397440	−2.67	0.06	−1.35	0.03	3(1)	−4.09	0.04	−2.09	0.02	3(1)	−1.42	0.07	−0.73	0.04
40	43200	−2.66	0.03	−1.36	0.02	4(1)	−4.05	0.04	−2.07	0.04	5(1)	−1.39	0.04	−0.72	0.04
40	397440	−2.76	0.05	−1.40	0.03	3(1)	−4.06	0.04	−2.06	0.02	3(1)	−1.30	0.06	−0.66	0.04
50	43200	−2.74	0.09	−1.39	0.05	5(1)	−4.06	0.11	−2.00	0.08	5(1)	−1.32	0.14	−0.61	0.09
50	397440	−2.88	0.08	−1.45	0.02	3(1)	−3.84	0.02	−1.96	0.01	3(1)	−0.96	0.09	−0.50	0.03
60	43200	−2.63	0.05	−1.35	0.02	4(1)	−4.05	0.09	−2.06	0.02	4(1)	−1.42	0.10	−0.71	0.03
60	397440	−2.84	0.05	−1.44	0.04	3(1)	−3.89	0.05	−1.99	0.03	3(1)	−1.05	0.07	−0.55	0.05
70	43200	−2.72	0.05	−1.38	0.03	4(1)	−4.02	0.02	−2.06	0.01	4(1)	−1.30	0.05	−0.68	0.03
70	397440	−2.96	0.04	−1.51	0.03	3(1)	−3.63	0.06	−1.85	0.02	3(1)	−0.67	0.07	−0.34.	0.04
80	43200	−2.69	0.03	−1.37	0.03	4(1)	−3.97	0.04	−2.03	0.05	4(1)	−1.28	0.05	−0.66	0.06
80	397440	−3.06	0.04	−1.56	0.00	3(1)	−3.79	0.02	−1.93	0.03	3(1)	−0.73	0.04	−0.37	0.03

[a] n denotes the total number of isotope analysis; N denotes the number of replicate.
[b] Test solution contains 0.8 µmol of Mg (HPS932001, δ^{26}Mg = −2.93 ± 0.14‰ by Li et al. 2011) and 0.8 µmol of $BaCl_2$.
[c] $Err\Delta^{26}Mg = [(Err\delta^{26}Mg_{solid})^2 + (Err\delta^{26}Mg_{soln})^2]^{1/2}$.
[d] $Err\Delta^{25}Mg = [(Err\delta^{25}Mg_{solid})^2 + (Err\delta^{25}Mg_{soln})^2]^{1/2}$.

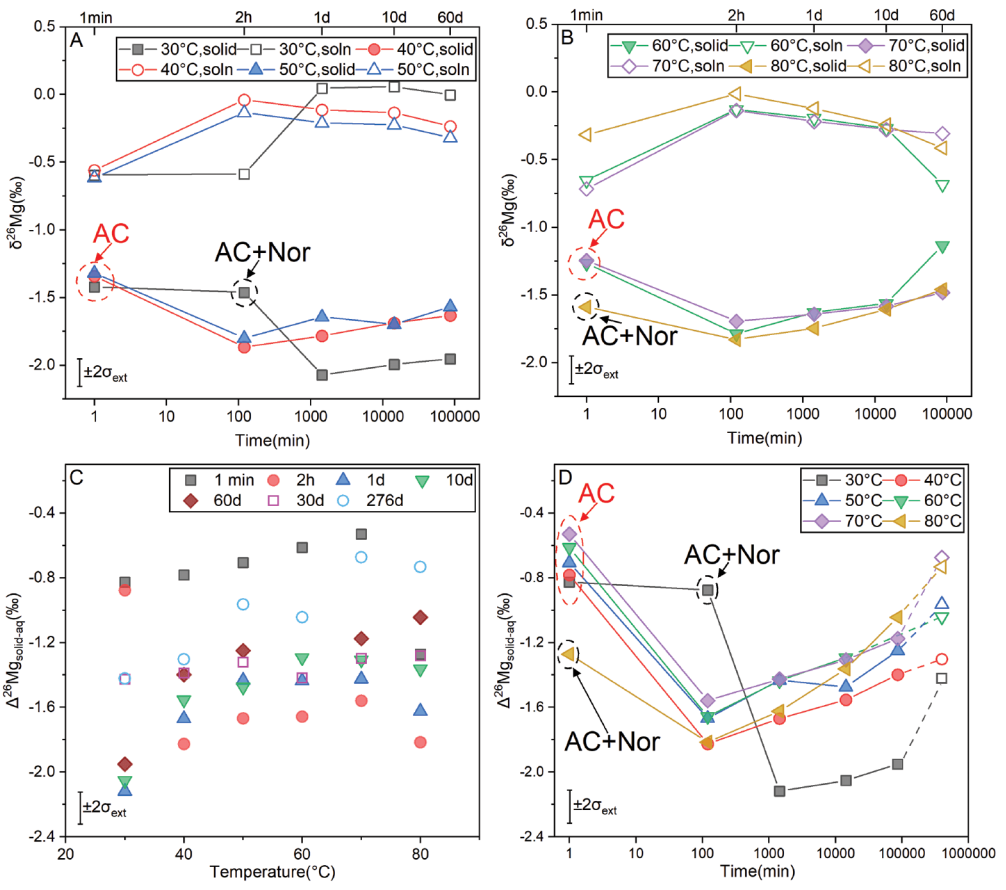

Figure 4. (**a**) $\delta^{26}Mg$ values of solid and aqueous phases vs. reaction time for experiments at 30 to 50 °C. (**b**) $\delta^{26}Mg$ values of solid and aqueous phases vs. reaction time for experiments at 60 to 80 °C. (**c**) $\Delta^{26}Mg_{solid\text{-}aq}$ vs. reaction temperature at different reaction times. (**d**) $\Delta^{26}Mg_{solid\text{-}aq}$ vs. reaction time at different temperatures. Solid dots represent the data for experiments Set I, while hollow dots represent the data for experiments Set II in **c** and **d**. AC = amorphous carbonate; Nor = norsethite. (Color online.)

which lead to the growth of larger crystals relative to experiments at higher temperatures. The $\Delta^{26}Mg_{solid\text{-}aq}$ fractionation factors decreased significantly during the transformation process (Figs. 4c and 4d). The remarkable decrease in $\Delta^{26}Mg_{solid\text{-}aq}$ after complete transformation of Ba-Mg amorphous carbonate can be attributed to the near-complete (100%) Mg isotope exchange during the transformation process, as rigorously proven using an enriched ^{25}Mg isotope tracer (Liu and Li 2020). However, it should be noted that the measured $\Delta^{26}Mg_{solid\text{-}aq}$ factors for the newly formed nano-norsethite (–2.12‰ to –1.56‰) were significantly lower than the calculated equilibrium Mg isotope fractionation factors for norsethite (–0.68‰ to –0.50‰; Fig. 5b). This indicates that the Mg isotope fractionation during a fast dissolution-reprecipitation process is kinetically controlled, which leads to depletion in heavy Mg isotopes in the mineral phase.

After Ba-Mg amorphous carbonate transformation, recrystallization of the nano-norsethite crystals proceeded with a longer reaction time. In this process, the norsethite crystal coarsened and developed rhombohedra crystal habit, which was accompanied by the disappearance of granular crystal shape (Figs. 2d–2i; Online Materials[1] Figs. S3 and S4). The decrease of d(104) may reflect the increase of Mg:Ba ratio in the norsethite due to the larger ionic radius of Ba relative to Mg, similar to the case of dolomite (Zhang et al. 2010). In the meantime, the FWHM of (104) peak of the norsethite decreased, indicating better crystallinity of the mineral over time. This is consistent with the common concept of recrystallization via Ostwald ripening during mineral-fluid interaction (Ratke and Voorhees 2002), which proceeds by a coupled dissolution-reprecipitation mechanism, as evidenced by the continuous decrease of SSA of solid products with longer reaction time (Fig. 1b). The measured $\Delta^{26}Mg_{solid\text{-}aq}$ factors increased with time for all experiments during this process (Figs. 4c and 4d) and approached the calculated equilibrium fractionation factors, which implies that the Mg exchange during this process was accompanied by the equilibrium fractionation. It is in agreement with a general concept that a slow dissolution-reprecipitation would drive the system to evolve toward equilibrium with time, as has been demonstrated in experiments on multiple metal isotopes in carbonate minerals (Mavromatis et al. 2016, 2017a; Oelkers et al. 2018, 2019; Pearce et al. 2012) and Mg isotopes for Mg-sulfate (Li et al. 2011). In addition to the dissolution-reprecipitation, the Mg isotope composition of minerals may be changed via the surface exchange or diffusion process (e.g., Huang et al. 2010; Richter et al. 2003, 2008; Teng et al. 2011). However, based on the SSA value, the calculated total amount of Mg at the surface only accounts for <3% of the total Mg in norsethite crystals (details in Online Materials[1] Appendix). Therefore, the surface process is not responsible for the significant increase of the $\delta^{26}Mg$ of norsethite. Moreover, diffusion of Mg ion in carbonate (Fisler and Cygan 1999; Kent et al. 2001) is too slow at the experimental temperatures in this study to influence the Mg isotope composition of norsethite (details in Online Materials[1] Appendix). Furthermore, the slight decreased Mg concentration during this process indicates the extra Mg mass transfer from solution to the solid phase,

TABLE 2. Optimized lattice parameters of norsethite and dolomite calculated from different exchange–correlation functionals compared with experiment measurements, as well as the reduced partition function ratios

Mineral		GGA	Error	LDA	Error	PBEsol	Error	Exp[a,b]
Norsethite	*a* (Å)	5.086	1.27%	4.987	−0.70%	5.038	0.32%	5.022
	c (Å)	16.916	0.87%	16.070	−4.17%	16.484	−1.71%	16.770
	V (Å^3)	379.02	3.48%	346.10	−5.51%	362.31	−1.08%	366.283
	$10^3\ln\beta$	$1.9424 \times 10^6/T^2$		$2.4507 \times 10^6/T^2$		$2.1855 \times 10^6/T^2$		
Dolomite	*a* (Å)	4.859	1.08%	4.770	−0.77%	4.818	0.23%	4.807
	c (Å)	16.179	1.11%	15.469	−3.33%	15.846	−0.97%	16.002
	V (Å^3)	330.83	3.32%	304.85	−4.79%	318.55	−0.52%	320.210
	$10^3\ln\beta$	$1.8653 \times 10^6/T^2$		$2.3782 \times 10^6/T^2$		$2.0902 \times 10^6/T^2$		
Magnesite	*a* (Å)	4.685	1.08	4.602	−0.71	4.649	0.30	4.635
	c (Å)	15.166	0.98	14.549	−3.13	14.873	−0.97	15.019
	V (Å^3)-	288.257	3.16	266.879	−4.49	278.419	−0.36	279.429
	$10^3\ln\beta$	$1.8177 \times 10^6/T^2$		$2.2204 \times 10^6/T^2$		$2.0254 \times 10^6/T^2$		
	$10^3\ln\alpha_{mag-dolo}$	$-0.0476 \times 10^6/T^2$		$-0.1578 \times 10^6/T^2$		$-0.0648 \times 10^6/T^2$		
	$10^3\ln\alpha_{nor-dolo}$	$0.0771 \times 10^6/T^2$		$0.0725 \times 10^6/T^2$		$0.0953 \times 10^6/T^2$		
	$10^3\ln\alpha_{nor-soln}$	$-0.0783 \times 10^6/T^2$		$-0.0829 \times 10^6/T^2$		$-0.0601 \times 10^6/T^2$		

[a] Norsethite (Effenberger and Zemann 1985).
[b] Dolomite and magnesite (Markgraf and Reeder 1985).

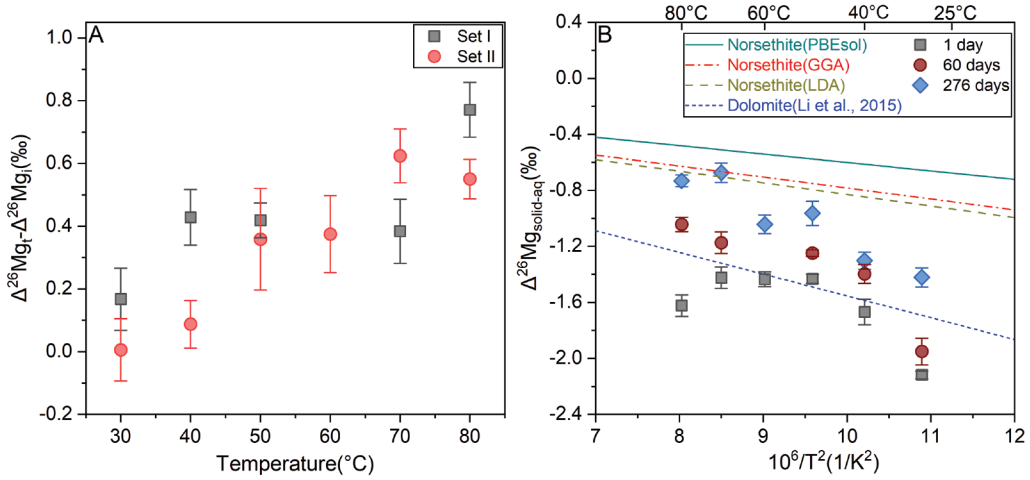

FIGURE 5. (**a**) The increase in measured $\Delta^{26}Mg_{solid-aq}$ fractionation factors vs. temperature, including data from experiment Set I (1 to 60 days), and data from experiment Set II (30 to 276 days). Error bar denotes 2 standard deviations. (**b**) Comparison of experimentally measured (points with error bars) and theoretically calculated (lines) $\Delta^{26}Mg$ factors for norsethite. The temperature-dependent Mg isotope fractionation factor for dolomite suggested by Li et al. (2015) is also plotted for reference. (Color online.)

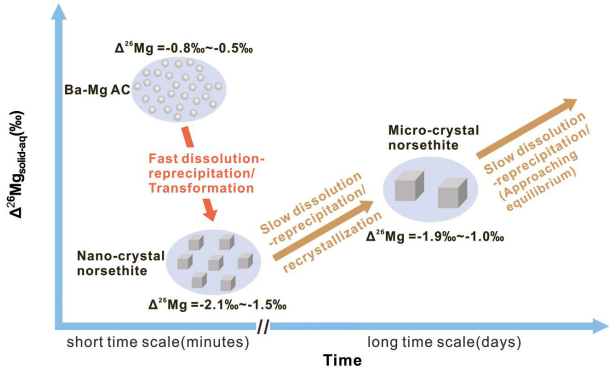

FIGURE 6. A schematic model showing the formation pathway of norsethite and the Mg isotopic fractionation behavior. (Color online.)

which can lead to the extra Mg isotope fractionation. Therefore, the mass transfer corrections were conducted (details in Online Materials[1] Appendix). This correction had limited influence on the increasing trend of Mg isotope fractionation with longer reaction time (Online Materials[1] Fig. S9). Notably, the magnitude of the increase in $\Delta^{26}Mg_{solid-aq}$ fractionation factors was greater for the experiments at higher temperatures, irrespective of experimental settings (experiment Set I or Set II; Fig. 5a). This can be attributed to continuous isotope exchange between norsethite crystals and aqueous solution in this stage, as exchange rates in reactions are positively temperature-dependent (Li et al. 2015).

IMPLICATIONS

Magnesium isotopes in marine carbonate have been applied to reconstruct the Mg isotopic and chemical composition of ancient seawater (Crockford et al. 2021; Fantle and Higgins 2014; Gothmann et al. 2017; Higgins and Schrag 2012; Hu et al. 2019; Li

et al. 2015, 2019; Pogge von Strandmann et al. 2014). However, the use of carbonates as an Mg isotope archive of seawater faces challenges, including: (1) to discern whether isotope equilibrium fractionation has been attained between the carbonate and seawater; and (2) to ascertain whether the Mg isotope records in carbonate are influenced by the post-depositional process. Our findings show that significant exchange of Mg between solid and solution occurs during recrystallization of norsethite via dissolution-reprecipitation, leading to the obvious alteration of Mg isotopic compositions. However, the incorporation of aqueous Mg^{2+} into carbonate minerals is not supported under ambient temperature due to the kinetic barrier of dehydration (Land 1998), and the dolomite precipitation is rare in the modern sedimentary environment (Warren 2000). By contrast, massive dolomite formation was found in the geological record (Burns et al. 2000; Given and Wilkinson 1987), which demonstrated that the Mg content and isotope composition of carbonate could be influenced by post-depositional processes. Meanwhile, the degree of the alteration of carbonate isotope composition is influenced by the reaction rate, duration of reaction, and the degree of isotopic disequilibrium (Chanda and Fantle 2017; Fantle 2015; Fantle et al. 2020; Huber et al. 2017). Therefore, various geological settings and post-depositional history of samples should be taken into consideration to potentially impact the recrystallization on Mg isotopic record in carbonates. For example, if a carbonate of marine origin remains in contact with seawater (i.e., "seawater buffered") for a protracted period of time, the continuous isotope exchange shall result in the Mg isotope re-equilibrium between carbonate and coeval seawater, and, therefore, seawater Mg isotope composition can be recorded (Li et al. 2015). However, sedimentary carbonates also underwent burial and related post-depositional processes, during which they reacted with isotopically evolved pore water or hydrothermal fluids, leading to further isotope exchange. If the fluids contain insufficient Mg relative to the carbonate, which is a so-called "sediment-buffered" environment, slow recrystallization of carbonate would take place, but the process will reset the Mg isotope composition of fluids rather than that of Mg-rich carbonates. It is a common case for carbon isotopes in carbonates (Swart 2015) but also for Mg isotopes in dolostone during the burial metamorphism (Azmy et al. 2013; Geske et al. 2012; Hu et al. 2017) or hydrothermal alteration (Geske et al. 2015; Hu et al. 2019).

A "fluid-buffered" situation could also take place for some carbonates during burial and subsequent post-depositional processes. If the amount of Mg in fluids was sufficient enough, the recrystallization would cause overprinting of Mg isotope signatures of carbonate while that of fluids evolves synchronously or remains relatively constant (e.g., Fantle and Higgins 2014; Huang et al. 2015). The greatest challenge in metal isotope studies of carbonate archives lies in distinguishing "sediment-buffered" and "fluid-buffered" situations, which would require applications of multiple geochemical tools to interrogate the fidelity of Mg isotopes in the studied carbonates (Riechelmann et al. 2020).

Our results provide new insights for applications of Mg isotopes in the carbonate archive. On the one hand, our study indicates that the amorphous carbonate transformation can lead to significant decrease of Mg isotope fractionation between the solid and solution phase. As a consequence, the Mg isotope fractionation between the newly formed crystalline carbonate minerals and surrounding solution could be more negative than equilibrium values from a single-stage precipitation, thus special attention is required in Mg isotope studies on biogenic carbonates. On the other hand, recrystallization has a great impact on the preservation of the initial isotope signature of crystalline carbonate, the extent to which this may influence the original isotopic signature depends on the type of diagenetic fluids and the relative Mg amount of carbonate and fluids.

Acknowledgments and Funding

This paper benefited from constructive comments from Carlos M. Pina and an anonymous reviewer, as well as editorial handling by Jianwei Wang on the earlier versions of the manuscript. This study was supported by the National Science Foundation (41873004, 41473002, 41622301) of China and the program A for Outstanding Ph.D. candidate of Nanjing University. We acknowledge the High Performance Computing Center (HPCC) of Nanjing University for doing the numerical calculations in this paper on its blade cluster system. We are grateful to Yuguan Pan for XRD analysis, Zhenmeng Sun, and Xiancai Lu for support in performing mineral SSA analysis, as well as Bei Huang for MC-ICP-MS operation. We also thank Zhiguang Xia for assistance in lab work.

References cited

Azmy, K., Lavoie, D., Wang, Z., Brand, U., Al-Aasm, I., Jackson, S., and Girard, I. (2013) Magnesium-isotope and REE compositions of Lower Ordovician carbonates from eastern Laurentia: Implications for the origin of dolomites and limestones. Chemical Geology, 356, 64–75.

Banner, J.L. (1995) Application of the trace-element and isotope geochemistry of strontium to studies of carbonate diagenesis. Sedimentology, 42, 805–824.

Baronnet, A., Cuif, J.P., Dauphin, Y., Farre, B., and Nouet, J. (2008) Crystallization of biogenic Ca-carbonate within organo-mineral micro-domains. Structure of the calcite prisms of the Pelecypod Pinctada margaritifera (Mollusca) at the submicron to nanometre ranges. Mineralogical Magazine, 72, 617–626.

Bialik, O.M., Wang, X., Zhao, S., Waldmann, N.D., Frank, R., and Li, W. (2018) Mg isotope response to dolomitization in hinterland-attached carbonate platforms: Outlook of δ^{26}Mg as a tracer of basin restriction and seawater Mg/Ca ratio. Geochimica et Cosmochimica Acta, 235, 189–207.

Bice, K.L., Birgel, D., Meyers, P.A., Dahl, K.A., Hinrichs, K.U., and Norris, R.D. (2006) A multiple proxy and model study of Cretaceous upper ocean temperatures and atmospheric CO_2 concentrations. Paleoceanography, 21, PA2002.

Bigeleisen, J., and Mayer, M.G. (1947) Calculation of equilibrium constants for isotopic exchange reactions. The Journal of Chemical Physics, 15, 261–267.

Børja, I., and Nilsen, P. (2009) Long term effect of liming and fertilization on ectomycorrhizal colonization and tree growth in old Scots pine (*Pinus sylvestris* L.) stands. Plant and Soil, 314, 109–119.

Burdige, D.J., Hu, X., and Zimmerman, R.C. (2010) The widespread occurrence of coupled carbonate dissolution/reprecipitation in surface sediments on the Bahamas Bank. American Journal of Science, 310, 492–521.

Burns, S.J., McKenzie, J.A., and Vasconcelos, C. (2000) Dolomite formation and biogeochemical cycles in the Phanerozoic. Sedimentology, 47, 49–61.

Chanda, P., and Fantle, M.S. (2017) Quantifying the effect of diagenetic recrystallization on the Mg isotopic composition of marine carbonates. Geochimica et Cosmochimica Acta, 204, 219–239.

Chanda, P., Gorski, C.A., Oakes, R.L., and Fantle, M.S. (2019) Low temperature stable mineral recrystallization of foraminiferal tests and implications for the fidelity of geochemical proxies. Earth and Planetary Science Letters, 506, 428–440.

Crockford, P.W., Kunzmann, M., Blättler, C.L., Kalderon-Asael, B., Murphy, J.G., Ahm, A.-S., Sharoni, S., Halverson, G.P., Planavsky, N.J., Halevy, I., and Higgins, J.A. (2021) Reconstructing Neoproterozoic seawater chemistry from early diagenetic dolomite. Geology, 49, 442–446.

Davis, K.J., Dove, P.M., and De Yoreo, J.J. (2000) The role of Mg^{2+} as an impurity in calcite growth. Science, 290, 1134–1137.

De Muynck, W., Debrouwer, D., De Belie, N., and Verstraete, W. (2008) Bacterial carbonate precipitation improves the durability of cementitious materials. Cement and Concrete Research, 38, 1005–1014.

De Yoreo, J.J., Waychunas, G.A., Jun, Y.-S., and Fernandez-Martinez, A. (2013) In situ investigations of carbonate nucleation on mineral and organic surfaces. Reviews in Mineralogy and Geochemistry, 77, 229–257.

Derry, L.A., Kaufman, A.J., and Jacobsen, S.B. (1992) Sedimentary cycling and environmental change in the Late Proterozoic: Evidence from stable and radiogenic isotopes. Geochimica et Cosmochimica Acta, 56, 1317–1329.

Effenberger, H., and Zemann, J. (1985) Single-crystal X-ray-investigation of norsethite, $BaMg(CO_3)_2$—one more mineral with an aplanar carbonate group. Zeitschrift für Kristallographie, 171, 275–280.

Effenberger, H., Pippinger, T., Libowitzky, E., Lengauer, C.L., and Miletich, R. (2014) Synthetic norsethite, $BaMg(CO_3)_2$: Revised crystal structure, thermal behaviour and

displacive phase transition. Mineralogical Magazine, 78, 1589–1611.
Fantle, M.S. (2015) Calcium isotopic evidence for rapid recrystallization of bulk marine carbonates and implications for geochemical proxies. Geochimica et Cosmochimica Acta, 148, 378–401.
Fantle, M.S., and Higgins, J. (2014) The effects of diagenesis and dolomitization on Ca and Mg isotopes in marine platform carbonates: Implications for the geochemical cycles of Ca and Mg. Geochimica et Cosmochimica Acta, 142, 458–481.
Fantle, M.S., Barnes, B.D., and Lau, K.V. (2020) The role of diagenesis in shaping the geochemistry of the marine carbonate record. Annual Review of Earth and Planetary Sciences, 48, 549–583.
Fisler, D.K., and Cygan, R.T. (1999) Diffusion of Ca and Mg in calcite. American Mineralogist, 84, 1392–1399.
Frierdich, A.J., Nebel, O., Beard, B.L., and Johnson, C.M. (2019) Iron isotope exchange and fractionation between hematite (α-Fe_2O_3) and aqueous Fe(II): A combined three-isotope and reversal-approach to equilibrium study. Geochimica et Cosmochimica Acta, 245, 207–221.
Gao, C., Cao, X., Liu, Q., Yang, Y., Zhang, S., He, Y., Tang, M., and Liu, Y. (2018) Theoretical calculation of equilibrium Mg isotope fractionations between minerals and aqueous solutions. Chemical Geology, 488, 62–75.
Gautier, Q., Bénézeth, P., Mavromatis, V., and Schott, J. (2014) Hydromagnesite solubility product and growth kinetics in aqueous solution from 25 to 75 °C. Geochimica et Cosmochimica Acta, 138, 1–20.
Gebauer, D., and Cölfen, H. (2011) Prenucleation clusters and non-classical nucleation. Nano Today, 6, 564–584.
Geske, A., Zorlu, J., Richter, D.K., Buhl, D., Niedermayr, A., and Immenhauser, A. (2012) Impact of diagenesis and low grade metamorphosis on isotope (δ^{26}Mg, δ^{13}C, δ^{18}O and $^{87}Sr/^{86}Sr$) and elemental (Ca, Mg, Mn, Fe and Sr) signatures of Triassic sabkha dolomites. Chemical Geology, 332-333, 45–64.
Geske, A., Goldstein, R.H., Mavromatis, V., Richter, D.K., Buhl, D., Kluge, T., John, C.M., and Immenhauser, A. (2015) The magnesium isotope (δ^{26}Mg) signature of dolomites. Geochimica et Cosmochimica Acta, 149, 131–151.
Giuffre, A.J., Gagnon, A.C., De Yoreo, J.J., and Dove, P.M. (2015) Isotopic tracer evidence for the amorphous calcium carbonate to calcite transformation by dissolution-reprecipitation. Geochimica et Cosmochimica Acta, 165, 407–417.
Given, R.K., and Wilkinson, B.H. (1987) Dolomite abundance and stratigraphic age; constraints on rates and mechanisms of Phanerozoic dolostone formation. Journal of Sedimentary Research, 57, 1068–1078.
Gorski, C.A., and Fantle, M.S. (2017) Stable mineral recrystallization in low temperature aqueous systems: A critical review. Geochimica et Cosmochimica Acta, 198, 439–465.
Gothmann, A.M., Stolarski, J., Adkins, J.F., and Higgins, J.A. (2017) A Cenozoic record of seawater Mg isotopes in well-preserved fossil corals. Geology, 45, 1039–1042.
Gower, L.B. (2008) Biomimetic model systems for investigating the amorphous precursor pathway and its role in biomineralization. Chemical Reviews, 108, 4551–4627.
Gu, C., Li, Q., Gu, Z., and Zhu, G. (2008) Study on application of CeO_2 and $CaCO_3$ nanoparticles in lubricating oils. Journal of Rare Earths, 26, 163–167.
Harrison, A.L., Mavromatis, V., Oelkers, E.H., and Bénézeth, P. (2019) Solubility of the hydrated Mg-carbonates nesquehonite and dypingite from 5 to 35 °C: Implications for CO_2 storage and the relative stability of Mg-carbonates. Chemical Geology, 504, 123–135.
Higgins, J.A., and Schrag, D.P. (2012) Records of Neogene seawater chemistry and diagenesis in deep-sea carbonate sediments and pore fluids. Earth and Planetary Science Letters, 357-358, 386–396.
Hofmann, A.E., Bourg, I.C., and DePaolo, D.J. (2012) Ion desolvation as a mechanism for kinetic isotope fractionation in aqueous systems. Proceedings of the National Academy of Sciences, 109, 18689–18694.
Hong, M., Xu, J., and Teng, H.H. (2016) Evolution of calcite growth morphology in the presence of magnesium: Implications for the dolomite problem. Geochimica et Cosmochimica Acta, 172, 55–64.
Hu, X., and Burdige, D.J. (2007) Enriched stable carbon isotopes in the pore waters of carbonate sediments dominated by seagrasses: Evidence for coupled carbonate dissolution and reprecipitation. Geochimica et Cosmochimica Acta, 71, 129–144.
Hu, Z., Hu, W., Wang, X., Lu, Y., Wang, L., Liao, Z., and Li, W. (2017) Resetting of Mg isotopes between calcite and dolomite during burial metamorphism: Outlook of Mg isotopes as geothermometer and seawater proxy. Geochimica et Cosmochimica Acta, 208, 24–40.
Hu, Z., Hu, W., Liu, C., Sun, F., Liu, Y., and Li, W. (2019) Conservative behavior of Mg isotopes in massive dolostones: From diagenesis to hydrothermal reworking. Sedimentary Geology, 381, 65–75.
Huang, F., Chakraborty, P., Lundstrom, C.C., Holmden, C., Glessner, J.J.G., Kieffer, S.W., and Lesher, C.E. (2010) Isotope fractionation in silicate melts by thermal diffusion. Nature, 464, 396–400.
Huang, K.-J., Shen, B., Lang, X.-G., Tang, W.-B., Peng, Y., Ke, S., Kaufman, A.J., Ma, H.-R., and Li, F.-B. (2015) Magnesium isotopic compositions of the Mesoproterozoic dolostones: Implications for Mg isotopic systematics of marine carbonates. Geochimica et Cosmochimica Acta, 164, 333–351.
Huber, C., Druhan, J.L., and Fantle, M.S. (2017) Perspectives on geochemical proxies: The impact of model and parameter selection on the quantification of carbonate recrystallization rates. Geochimica et Cosmochimica Acta, 217, 171–192.
Jacob, D.E., Wirth, R., Agbaje, O.B.A., Branson, O., and Eggins, S.M. (2017) Planktic foraminifera form their shells via metastable carbonate phases. Nature Communications, 8, 1265.
Jin, D., and Yue, L. (2008) Tribological properties study of spherical calcium carbonate composite as lubricant additive. Materials Letters, 62, 1565–1568.
Kent, A.J.R., Hutcheon, I.D., Ryerson, F.J., and Phinney, D.L. (2001) The temperature of formation of carbonate in martian meteorite ALH84001: Constraints from cation diffusion. Geochimica et Cosmochimica Acta, 65, 311–321.
Kresse, G., and Joubert, D. (1999) From ultrasoft pseudopotentials to the projector augmented-wave method. Physical Review B, 59, 1758–1775.
Lachniet, M.S. (2009) Climatic and environmental controls on speleothem oxygen-isotope values. Quaternary Science Reviews, 28, 412–432.
Lam, R.S.K., Charnock, J.M., Lennie, A., and Meldrum, F.C. (2007) Synthesis-dependant structural variations in amorphous calcium carbonate. CrystEngComm, 9, 1226–1236.
Land, L.S. (1998) Failure to precipitate dolomite at 25 °C from dilute solution despite 1000-fold oversaturation after 32 years. Aquatic Geochemistry, 4, 361–368.
Li, W., Beard, B.L., and Johnson, C.M. (2011) Exchange and fractionation of Mg isotopes between epsomite and saturated $MgSO_4$ solution. Geochimica et Cosmochimica Acta, 75, 1814–1828.
Li, W., Beard, B.L., Li, C., Xu, H., and Johnson, C.M. (2015) Experimental calibration of Mg isotope fractionation between dolomite and aqueous solution and its geological implications. Geochimica et Cosmochimica Acta, 157, 164–181.
Li, W., Bialik, O.M., Wang, X., Yang, T., Hu, Z., Huang, Q., Zhao, S., and Waldmann, N.D. (2019) Effects of early diagenesis on Mg isotopes in dolomite: The roles of Mn(IV)-reduction and recrystallization. Geochimica et Cosmochimica Acta, 250, 1–17.
Lin, C.-J., Yang, S.-Y., Huang, S.-J., and Chan, J.C.C. (2015) Structural characterization of Mg-stabilized amorphous calcium carbonate by Mg-25 solid-state NMR spectroscopy. The Journal of Physical Chemistry C, 119, 7225–7233.
Lindner, M., and Jordan, G. (2018) On the growth of witherite and its replacement by the Mg-bearing double carbonate norsethite: Implications for the dolomite problem. American Mineralogist, 103, 252–259.
Lindner, M., Saldi, G.D., Carrocci, S., Benezeth, P., Schott, J., and Jordan, G. (2018) On the growth of anhydrous Mg-bearing carbonates – Implications from norsethite growth kinetics. Geochimica et Cosmochimica Acta, 238, 424–437.
Liu, C., and Li, W. (2020) Transformation of amorphous precursor to crystalline carbonate: Insights from Mg isotopes in the dolomite-analogue mineral norsethite [$BaMg(CO_3)_2$]. Geochimica et Cosmochimica Acta, 272, 1–20.
Liu, C., Wang, Z., and Macdonald, F.A. (2018) Sr and Mg isotope geochemistry of the basal Ediacaran cap limestone sequence of Mongolia: Implications for carbonate diagenesis, mixing of glacial meltwaters, and seawater chemistry in the aftermath of Snowball Earth. Chemical Geology, 491, 1–13.
Loste, E., Wilson, R.M., Seshadri, R., and Meldrum, F.C. (2003) The role of magnesium in stabilising amorphous calcium carbonate and controlling calcite morphologies. Journal of Crystal Growth, 254, 206–218.
Markgraf, S.A., and Reeder, R.J. (1985) High-temperature structure refinements of calcite and magnesite. American Mineralogist, 70, 590–600.
Mass, T., Giuffre, A.J., Sun, C.-Y., Stifler, C.A., Frazier, M.J., Neder, M., Tamura, N., Stan, C.V., Marcus, M.A., and Gilbert, P.U.P.A. (2017) Amorphous calcium carbonate particles form coral skeletons. Proceedings of the National Academy of Sciences, 114, E7670–E7678.
Mavromatis, V., van Zuilen, K., Purgstaller, B., Baldermann, A., Nagler, T.F., and Dietzel, M. (2016) Barium isotope fractionation during witherite ($BaCO_3$) dissolution, precipitation and at equilibrium. Geochimica et Cosmochimica Acta, 190, 72–84.
Mavromatis, V., Harrison, A.L., Eisenhauer, A., and Dietzel, M. (2017a) Strontium isotope fractionation during strontianite ($SrCO_3$) dissolution, precipitation and at equilibrium. Geochimica et Cosmochimica Acta, 218, 201–214.
Mavromatis, V., Purgstaller, B., Dietzel, M., Buhl, D., Immenhauser, A., and Schott, J. (2017b) Impact of amorphous precursor phases on magnesium isotope signatures of Mg-calcite. Earth and Planetary Science Letters, 464, 227–236.
McDermott, F. (2004) Palaeo-climate reconstruction from stable isotope variations in speleothems: a review. Quaternary Science Reviews, 23, 901–918.
Mitsuguchi, T., Matsumoto, E., Abe, O., Uchida, T., and Isdale, P.J. (1996) Mg/Ca thermometry in coral skeletons. Science, 274, 961 –963.
Monkhorst, H.J., and Pack, J.D. (1976) Special points for Brillouin-zone integrations. Physical Review B, 13, 5188–5192.
Mor Khalifa, G., Kahil, K., Erez, J., Kaplan Ashiri, I., Shimoni, E., Pinkas, I., Addadi, L., and Weiner, S. (2018) Characterization of unusual MgCa particles involved in the formation of foraminifera shells using a novel quantitative cryo SEM/EDS protocol. Acta Biomaterialia, 77, 342–351.
Morse, J.W., and Mackenzie, F.T. (1990) Geochemistry of Sedimentary Carbonates, 706 p. Elsevier Science.
Nielsen, M.R., Sand, K.K., Rodriguez-Blanco, J.D., Bovet, N., Generosi, J., Dalby, K.N., and Stipp, S.L.S. (2016) Inhibition of calcite growth: Combined effects of Mg^{2+} and SO_4^{2-}. Crystal Growth & Design, 16, 6199–6207.
Oelkers, E.H., Berninger, U.-N., Perez-Fernandez, A., Chmeleff, J., and Mavromatis, V. (2018) The temporal evolution of magnesium isotope fractionation during hydromagnesite dissolution, precipitation, and at equilibrium. Geochimica et Cosmochimica Acta, 226, 36–49.
Oelkers, E.H., von Strandmann, P.A.E.P., and Mavromatis, V. (2019) The rapid resetting

of the Ca isotopic signatures of calcite at ambient temperature during its congruent dissolution, precipitation, and at equilibrium. Chemical Geology, 512, 1–10.
Pearce, C.R., Saldi, G.D., Schott, J., and Oelkers, E.H. (2012) Isotopic fractionation during congruent dissolution, precipitation and at equilibrium: Evidence from Mg isotopes. Geochimica et Cosmochimica Acta, 92, 170–183.
Perdew, J.P., and Zunger, A. (1981) Self-interaction correction to density-functional approximations for many-electron systems. Physical Review B, 23, 5048–5079.
Perdew, J.P., Burke, K., and Ernzerhof, M. (1996) Generalized gradient approximation made simple. Physical Review Letters, 77, 3865–3868.
Perdew, J.P., Ruzsinszky, A., Csonka, G.I., Vydrov, O.A., Scuseria, G.E., Constantin, L.A., Zhou, X., and Burke, K. (2008) Restoring the density-gradient expansion for exchange in solids and surfaces. Physical Review Letters, 100, 136406.
Pimentel, C., and Pina, C.M. (2014) The formation of the dolomite-analogue norsethite: Reaction pathway and cation ordering. Geochimica et Cosmochimica Acta, 142, 217–223.
——— (2016) Reaction pathways towards the formation of dolomite-analogues at ambient conditions. Geochimica et Cosmochimica Acta, 178, 259–267.
Pimentel, C., Pina, C.M., and Sainz-Díaz, C.I. (2021) DFT simulations of the structure and cation order of norsethite, $BaMg(CO_3)_2$. ACS Earth and Space Chemistry, 5, 1486–1497.
Pinilla, C., Blanchard, M., Balan, E., Natarajan, S.K., Vuilleumier, R., and Mauri, F. (2015) Equilibrium magnesium isotope fractionation between aqueous Mg^{2+} and carbonate minerals: Insights from path integral molecular dynamics. Geochimica et Cosmochimica Acta, 163, 126–139.
Pogge von Strandmann, P.A.E., Forshaw, J., and Schmidt, D.N. (2014) Modern and Cenozoic records of seawater magnesium from foraminiferal Mg isotopes. Biogeosciences, 11, 5155–5168.
Politi, Y., Metzler, R.A., Abrecht, M., Gilbert, B., Wilt, F.H., Sagi, I., Addadi, L., Weiner, S., and Gilbert, P.U.P.A. (2008) Transformation mechanism of amorphous calcium carbonate into calcite in the sea urchin larval spicule. Proceedings of the National Academy of Sciences, 105(50), 17362–17366.
Purgstaller, B., Mavromatis, V., Immenhauser, A., and Dietzel, M. (2016) Transformation of Mg-bearing amorphous calcium carbonate to Mg-calcite—In situ monitoring. Geochimica et Cosmochimica Acta, 174, 180–195.
Purgstaller, B., Konrad, F., Dietzel, M., Immenhauser, A., and Mavromatis, V. (2017) Control of Mg^{2+}/Ca^{2+} activity ratio on the formation of crystalline carbonate minerals via an amorphous precursor. Crystal Growth & Design, 17, 1069–1078.
Purgstaller, B., Goetschl, K.E., Mavromatis, V., and Dietzel, M. (2019) Solubility investigations in the amorphous calcium magnesium carbonate system. CrystEngComm, 21, 155–164.
Radha, A.V., and Navrotsky, A. (2013) Thermodynamics of carbonates. Reviews in Mineralogy and Geochemistry, 77, 73–121.
Rae, J.W.B., Foster, G.L., Schmidt, D.N., and Elliott, T. (2011) Boron isotopes and B/Ca in benthic foraminifera: Proxies for the deep ocean carbonate system. Earth and Planetary Science Letters, 302, 403–413.
Raiteri, P., and Gale, J.D. (2010) Water is the key to nonclassical nucleation of amorphous calcium carbonate. Journal of the American Chemical Society, 132, 17623–17634.
Ratke, L., and Voorhees, P.W. (2002) Growth and Coarsening Ostwald Ripening in Material Processing, 298 p. Springer.
Raz, S., Hamilton, P.C., Wilt, F.H., Weiner, S., and Addadi, L. (2003) The transient phase of amorphous calcium carbonate in sea urchin larval spicules: The involvement of proteins and magnesium ions in its formation and stabilization. Advanced Functional Materials, 13, 480–486.
Reeder, R.J., and Markgraf, S.A. (1986) High-temperature crystal chemistry of dolomite. American Mineralogist, 71, 795–804.
Reeves, D., and Rothman, D.H. (2013) Age dependence of mineral dissolution and precipitation rates. Global Biogeochemical Cycles, 27, 906–919.
Richter, F.M., Davis, A.M., DePaolo, D.J., and Watson, E.B. (2003) Isotope fractionation by chemical diffusion between molten basalt and rhyolite. Geochimica et Cosmochimica Acta, 67, 3905–3923.
Richter, F.M., Watson, E.B., Mendybaev, R.A., Teng, F.-Z., and Janney, P.E. (2008) Magnesium isotope fractionation in silicate melts by chemical and thermal diffusion. Geochimica et Cosmochimica Acta, 72, 206–220.
Riechelmann, S., Mavromatis, V., Buhl, D., Dietzel, M., and Immenhauser, A. (2020) Controls on formation and alteration of early diagenetic dolomite: A multi-proxy $\delta^{44/40}Ca$, $\delta^{26}Mg$, $\delta^{18}O$ and $\delta^{13}C$ approach. Geochimica et Cosmochimica Acta, 283, 167–183.
Ries, J.B. (2004) Effect of ambient Mg/Ca ratio on Mg fractionation in calcareous marine invertebrates: A record of the oceanic Mg/Ca ratio over the Phanerozoic. Geology, 32, 981–984.
Rodriguez-Blanco, J.D., Shaw, S., Bots, P., Roncal-Herrero, T., and Benning, L.G. (2012) The role of pH and Mg on the stability and crystallization of amorphous calcium carbonate. Journal of Alloys and Compounds, 536, S477–S479.
Rodriguez-Blanco, J.D., Sand, K.K., and Benning, L.G. (2017) ACC and vaterite as intermediates in the solution-based crystallization of $CaCO_3$. In A.E.S. Van Driessche, M.Kellermeier, L.G. Benning, and D. Gebauer, Eds., New Perspectives on Mineral Nucleation and Growth: From Solution Precursors to Solid Materials, p. 93–111. Springer.
Rollion-Bard, C., Blamart, D., Trebosc, J., Tricot, G., Mussi, A., and Cuif, J.-P. (2011) Boron isotopes as pH proxy: A new look at boron speciation in deep-sea corals using ^{11}B MAS NMR and EELS. Geochimica et Cosmochimica Acta, 75, 1003–1012.
Schott, J., Mavromatis, V., Fujii, T., Pearce, C.R., and Oelkers, E.H. (2016) The control of carbonate mineral Mg isotope composition by aqueous speciation: Theoretical and experimental modeling. Chemical Geology, 445, 120–134.
Sun, Z.M., Lu, X.C., Jia, X.C., Bai, Y.S., and Hu, W.X. (2017) Optimization of mercury intrusion capillary pressure measurement for characterizing the pore structure of tight rocks. Journal of Nanoscience and Nanotechnology, 17, 6242–6251.
Sun, C.-Y., Stifler, C.A., Chopdekar, R.V., Schmidt, C.A., Parida, G., Schoeppler, V., Fordyce, B.I., Brau, J.H., Mass, T., Tambutté, S., and Gilbert, P.U.P.A. (2020) From particle attachment to space-filling coral skeletons. Proceedings of the National Academy of Sciences, 117, 30159 –30170.
Swanson, S.E. (1977) Relation of nucleation and crystal-growth rate to the development of granitic textures. American Mineralogist, 62, 966–978.
Swart, P.K. (2015) The geochemistry of carbonate diagenesis: The past, present and future. Sedimentology, 62, 1233–1304.
Teng, H.H., Dove, P.M., and De Yoreo, J.J. (2000) Kinetics of calcite growth: surface processes and relationships to macroscopic rate laws. Geochimica et Cosmochimica Acta, 64, 2255–2266.
Teng, F.-Z., Dauphas, N., Helz, R.T., Gao, S., and Huang, S. (2011) Diffusion-driven magnesium and iron isotope fractionation in Hawaiian olivine. Earth and Planetary Science Letters, 308, 317–324.
Togo, A., and Tanaka, I. (2015) First principles phonon calculations in materials science. Scripta Materialia, 108, 1–5.
Urey, H.C. (1947) The thermodynamic properties of isotopic substances. Journal of the Chemical Society (Resumed), 562–581.
Von Euw, S., Zhang, Q., Manichev, V., Murali, N., Gross, J., Feldman, L.C., Gustafsson, T., Flach, C., Mendelsohn, R., and Falkowski, P.G. (2017) Biological control of aragonite formation in stony corals. Science, 356, 933 –938.
Wang, Y.J., Cheng, H., Edwards, R.L., An, Z.S., Wu, J.Y., Shen, C.C., and Dorale, J.A. (2001) A high-resolution absolute-dated Late Pleistocene Monsoon Record from Hulu Cave, China. Science, 294, 2345–2348.
Wang, Y., Yao, Z., Zhan, Y., Zheng, X., Zhou, M., Yan, G., Wang, L., Werner, C., and Butterbach-Bahl, K. (2021) Potential benefits of liming to acid soils on climate change mitigation and food security. Global Change Biology, 27, 2807–2821.
Warren, J. (2000) Dolomite: Occurrence, evolution and economically important associations. Earth-Science Reviews, 52, 1–81.
Weiss, I.M., Tuross, N., Addadi, L., and Weiner, S. (2002) Mollusc larval shell formation: Amorphous calcium carbonate is a precursor phase for aragonite. The Journal of Experimental Zoology, 293, 478–491.
Xu, X.R., Han, J.T., and Cho, K. (2004) Formation of amorphous calcium carbonate thin films and their role in biomineralization. Chemistry of Materials, 16, 1740–1746.
Zamanian, K., Pustovoytov, K., and Kuzyakov, Y. (2016) Recrystallization of shell carbonate in soil: ^{14}C labeling, modeling and relevance for dating and paleoreconstructions. Geoderma, 282, 87–95.
Zhang, F., Xu, H., Konishi, H., and Roden, E.E. (2010) A relationship between d_{104} value and composition in the calcite-disordered dolomite solid-solution series. American Mineralogist, 95, 1650–1656.
Zhang, F., Algeo, T.J., Romaniello, S.J., Cui, Y., Zhao, L., Chen, Z.-Q., and Anbar, A.D. (2018) Congruent Permian-Triassic $\delta^{238}U$ records at Panthalassic and Tethyan sites: Confirmation of global-oceanic anoxia and validation of the U-isotope paleoredox proxy. Geology, 46, 327–330.
Zhang, Y.-F., Yao, Q.-Z., Qian, F.-J., Li, H., Zhou, G.-T., and Fu, S.-Q. (2021) Formation pathway of norsethite dominated by solution chemistry under ambient conditions. American Mineralogist, 106, 1306–1318.
Zhu, C., Donald Rimstidt, J., Zhang, Y., Kang, J., Schott, J., and Yuan, H. (2020) Decoupling feldspar dissolution and precipitation rates at near-equilibrium with Si isotope tracers: Implications for modeling silicate weathering. Geochimica et Cosmochimica Acta, 271, 132–153.

Manuscript received November 14, 2021
Manuscript accepted February 6, 2022
Accepted manuscript online February 17, 2022
Manuscript handled by Jianwei Wang

Endnote:

[1]Deposit item AM-23-28386, Online Materials. Deposit items are free to all readers and found on the MSA website, via the specific issue's Table of Contents (go to http://www.minsocam.org/MSA/AmMin/TOC/2023/Feb2023_data/Feb2023_data.html).